



Tripple Doppler radar analysis of the heavy rain event observed in Lago Maggiore region during MAP IOP 2B

Jean-François Georgis, Frank Roux, Michel Chong, Stéphanie Pradier

► To cite this version:

Jean-François Georgis, Frank Roux, Michel Chong, Stéphanie Pradier. Tripple Doppler radar analysis of the heavy rain event observed in Lago Maggiore region during MAP IOP 2B. Quarterly Journal of the Royal Meteorological Society, 2003, 129, pp.495-522. 10.1256/qj.02.46 . hal-00137511

HAL Id: hal-00137511

<https://hal.science/hal-00137511>

Submitted on 12 Aug 2021

HAL is a multi-disciplinary open access archive for the deposit and dissemination of scientific research documents, whether they are published or not. The documents may come from teaching and research institutions in France or abroad, or from public or private research centers.

L'archive ouverte pluridisciplinaire **HAL**, est destinée au dépôt et à la diffusion de documents scientifiques de niveau recherche, publiés ou non, émanant des établissements d'enseignement et de recherche français ou étrangers, des laboratoires publics ou privés.



Distributed under a Creative Commons Attribution 4.0 International License

Triple-Doppler radar analysis of the heavy rain event observed in the Lago Maggiore region during MAP IOP 2b

By JEAN-FRANÇOIS GEORGIS*, FRANK ROUX, MICHEL CHONG and STEPHANIE PRADIER
Laboratoire d'Aérodologie, CNRS and Université Paul Sabatier, Toulouse, France

This paper presents analyses of data collected with three ground-based Doppler radars during the Mesoscale Alpine Programme (MAP) Intensive Observation Period (IOP) 2b from 1900 UTC 19 September until 1100 UTC 20 September 1999. During this period, the synoptic situation was characterized by the propagation of a deep upper-tropospheric trough towards the Alps, as often observed when heavy precipitation occurs on the southern slopes of the Alpine massif. A frontal cloud system with embedded convective cells passed over northern Italy in association with the trough moving rapidly eastwards. Ahead of the advancing cold front, a strong south to south-easterly low-level flow impinged on the mountains near Lago Maggiore and produced copious amounts of rain (>200 mm at several locations).

An analysis of three-dimensional radar-derived wind and precipitation fields shows that the most intense precipitation occurred where and when the easterly component of the low- to mid-level flow was the strongest with, however, a preferential location on the southern slopes of the Alps. This phenomenon can be explained by enhanced confluence between the main southerly flow and an intensifying easterly flow, and/or more favourable orientation of the moist inflow perpendicular to the mountain slopes. In addition, the propagation of convective cells from the Po Valley toward the Alps led to enhanced precipitation over the mountainous area.

Taking advantage of the approximately two-dimensional character of the event, the different terms of the water budget are calculated for a series of 25 successive vertical cross-sections to analyse the transformation of atmospheric moisture into surface rainfall.

KEYWORDS: Mesoscale Alpine Programme Multi-Doppler analyses Orographic precipitation Radar observations Water budget

1. INTRODUCTION

Because of its unique geographical aspects which largely control local weather events, the western Mediterranean region delimited by eastern Spain, southern France, northern Italy and northern Africa is frequently affected by heavy rain events, especially during autumn. In this season, the relatively warm sea surface acts as a moisture and heat source which is a primordial ingredient for the generation of heavy precipitation, provided a strong synoptic and/or local forcing exist. In these conditions, a moist low-level jet can settle in when a short-wave trough approaches this area. Through a diagnostic study of three heavy precipitation episodes in the western Mediterranean region, Doswell *et al.* (1998) showed that all of them occurred downstream of a significant cyclone aloft, as well as in the presence of steep mountains bordering the western Mediterranean sea, as the Atlas in north-western Africa, the Sierra Nevada in Spain, the Pyrenees between Spain and France and the south-western part of the Alps, which significantly modify the atmospheric flow. Depending on environmental static stability, Coriolis effect, flow velocity and geometry of the terrain, a situation of either 'flow over' or 'flow around/along' the obstacle can prevail. In the first configuration, orographic precipitation results from the lifting of moist low-level air along the mountain slope up to its condensation level. In the second case, the generation of precipitation is related to the presence of convergence zones resulting from the deflection of the low-level airflow by the mountains. Further information about the triggering mechanisms of orographic precipitation can be found in Smith (1979, 1989) and Houze (1993).

* Corresponding author: Laboratoire d'Aérodologie, Observatoire Midi-Pyrénées, 14 avenue Edouard Belin, 31400 Toulouse, France. e-mail: geojf@aero.obs-mip.fr

The southern Alpine regions are particularly affected by orographic precipitation and floods. During the last decade, several flash flood events resulting from heavy orographic rainfall have caused significant loss of life and damage to properties. Although most of them were convective events, such as the Vaison-la-Romaine flood of 22 September 1992 in France, the Brig flood of 24 September 1993 and the south Ticino flood of 13–14 September 1995 in Switzerland, more stratiform situations such as the Piedmont flood (PF) of 4–6 November 1994 in Italy, can also be destructive (e.g. Buzzi and Foschini 2000). Buzzi *et al.* (1998) discussed the crucial role of orography in determining distribution and amount of precipitation during the PF. Lin *et al.* (2001) have also shown that a concave mountain geometry, such as the Alps in the Ticino and Lago Maggiore region in north-western Italy, plays an important role in triggering heavy orographic rainfall since the resulting convergence of the low- to mid-level flow enhances upward motion along mountain slopes and produces heavier precipitation. This probably explains why precipitation associated with the majority of Alpine heavy orographic rainfall events often starts in this concave region south of the Alps (Binder and Schär 1996; Buzzi and Foschini 2000).

The convective events in Alpine regions are characterized by relatively low convective available potential energy (CAPE) values, as compared to those associated with thunderstorm outbreaks over flat continental areas. But, since they frequently occur downstream from an approaching deep short-wave trough, Lin *et al.* (2001) hypothesized that the enhancement of low-level upward motions caused by upper-level divergence and reduced static stability below the trough may partially compensate for a low CAPE value. Furthermore, as shown by Doswell *et al.* (1996), the persistence of rainfall is a more important factor than convection intensity. This is why even stratiform precipitation generated by persistent terrain-induced forced ascent can constitute a serious weather hazard.

Unfortunately, heavy rainfall events are difficult to forecast due to nonlinear flow dynamics and microphysics, and to the multiple length-scales of the terrain (e.g. Smith 1979). Thus, a better knowledge of the role of orography in the triggering and/or the intensification of precipitation is necessary to improve the forecasting of heavy rain location, intensity and duration. This was one of the main objectives of the Mesoscale Alpine Programme (MAP), the Special Observing Period (SOP) of which took place in the Alps in autumn 1999 (Bougeault *et al.* 2001). During this period, three ground-based Doppler radars were operated in the Lago Maggiore region to collect data for detailed analyses of wind and precipitation over mountainous terrain.

In this paper, we present a triple-Doppler radar analysis of Intensive Observation Period (IOP) 2b (18–21 September 1999) of MAP, during which a frontal cloud system with embedded convective elements passed over northern Italy in association with a trough moving rapidly eastwards over northern Europe.

IOP 2b was selected because it concerned the most intense heavy rain event observed over the Lago Maggiore region during the SOP (Bougeault *et al.* 2001) and exhibits characteristics comparable with previous flooding episodes. It was characterized by persistent rainfall from 1200 UTC 19 September (local time is UTC + 2 h) until 1800 UTC 20 September. Rain amounts in excess of 200 mm day⁻¹ were observed locally at various locations in the Lago Maggiore region. More than 300 mm in less than 30 h and a 10-minute rainfall intensity maximum of about 45 mm h⁻¹ were also recorded near the Toce Valley. Also, we propose to better explain in this paper why and how heavy precipitation is favoured in the Piedmont region. For that, we take advantage of Doppler data which can provide simultaneous information on the wind and precipitation fields with mesoscale coverage and convective-scale resolution. A triple-Doppler analysis is

carried out in order to benefit from a maximum extended areal coverage, and to mitigate possible errors in the retrieved three-dimensional precipitation and wind fields which are likely to be induced by eventual deficient radar data. Complementary analyses of Doppler radar data relative to IOP 2b can be found in Houze and Medina (2001) and Medina and Houze (2003). In both those studies, there is special emphasis on polarimetric observations in order to investigate the role of microphysics in the orographic convective precipitation maximum.

In section 2, the synoptic and mesoscale environmental features conducive to this heavy orographic rainfall event are discussed, and compared with those observed during previous flooding events in autumn over the southern slopes of the Alps. Section 3 presents a space–time analysis of the precipitating system observed by the three ground-based Doppler radars between 1900 UTC 19 September and 1100 UTC 20 September 1999, and a small-scale analysis of the three-dimensional wind and precipitation fields is carried out in order to better emphasize the local orographic effects on the spatial distribution of rainfall. In section 4, the rainfall amount is estimated from the reflectivity data and compared with rain-gauge measurements over the Lago-Maggiore region. Finally, the different elements of the water budget are estimated and discussed for a series of two-dimensional vertical cross-sections. Conclusions follow in section 5.

2. SYNOPSIS OF THE IOP 2B EVENT

(a) *Synoptic situation*

The synoptic situation prevailing during IOP 2b was remarkably similar to that observed during previous autumn flooding events on the southern slopes of the European Alps. It was characterized by a well-marked upper-level anomaly of potential vorticity (PV), which took the form of a north–south elongated band of high-PV air extending from west of Ireland to Spain and slowly moving toward the Alps. According to Massacand *et al.* (1998) who analysed the meteorological conditions of severe flooding situations during Alpine events, this high-PV band constitutes an upper-level precursor of heavy precipitation south of the Alps.

Among comparable events, the PF of November 1994 (Buzzi *et al.* 1998, Ferretti *et al.* 2000) presented the most synoptic characteristics similar to those of IOP 2b. In both cases a few hours before the period of intense precipitation a cyclone was located west of Ireland. At 0000 UTC 19 September 1999, a deep and cold baroclinic trough at 500 hPa (Fig. 1(a)) extending from the low centre to Spain progressively tilted south-eastwards and slowly moved eastwards. As a consequence, the associated cyclonic flow caused a progressively intensifying south-westerly jet over the western Mediterranean Sea. This resulted from the intensification of the geopotential gradient owing to the eastward progression of the trough and to the relatively stationary ridge which extended to the east from the central Mediterranean to Scandinavia, in the manner suggested previously for the PF by Buzzi *et al.* (1998). Hence, the warm tongue at 850 hPa (not shown, but recognizable in the 500 hPa temperature depicted in Fig. 1(b)) shrank in the zonal direction over Italy, ahead of the cold front (i.e. the zone of strong temperature contrast in Fig. 1(b)) which extended from south-east Spain to north-east France at 0000 UTC 20 September.

Meanwhile, the south-easterly flow in the lowest 10 m above the surface associated with the high pressure zone over eastern Europe underwent a westward deflection by the Alpine barrier, as it passed from the Adriatic sea to the Po Valley in northern Italy. As a result, a zone of convergence between this easterly flow and the southerly flow associated with the trough appeared over the western Po Valley, in the Piedmont

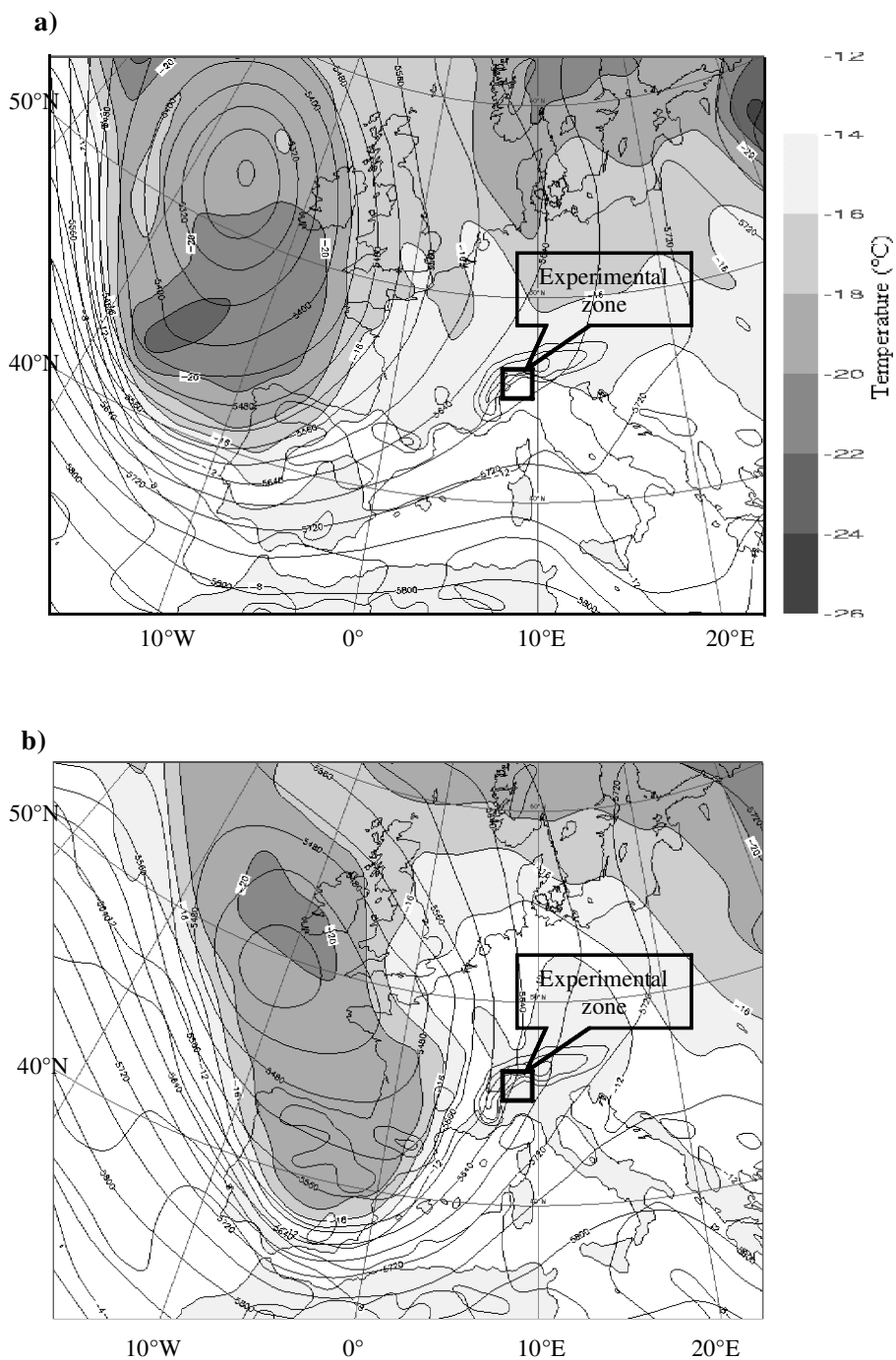


Figure 1. 500 hPa geopotential height (contours every 40 m) and temperature values (grey scale) at: (a) 0000 UTC 19 September, (b) 0000 UTC 20 September 1999, from the European Centre for Medium-Range Weather Forecasts 12 h forecasts.

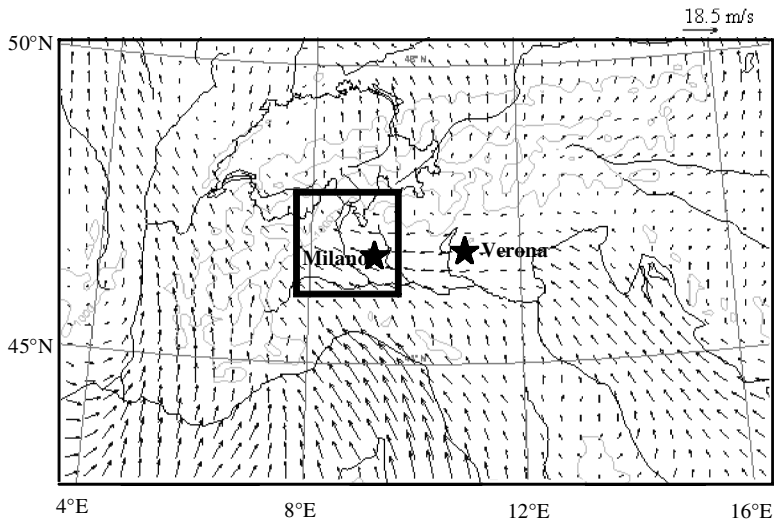


Figure 2. Swiss model analysed winds at 10 m altitude over Alpine regions at 0000 UTC 20 September 1999. The Lago Maggiore region is also shown.

region (Fig. 2). This convergence was observed from 1200 UTC 19 September until 1200 UTC 20 September, with a maximum intensity around 0000 UTC 20 September. Such conditions were obviously very favourable for the development of precipitation, provided the air mass was sufficiently moist. Furthermore, the easterly flow over the Po Valley slowed the eastward propagation of the front, which increased the duration of orographic precipitation over the southern slopes of the Alps, as has been documented for other events (Ferretti *et al.* 2000; Rotunno and Ferretti 2001).

(b) Mesoscale characteristics

In the PF case, the environmental flow was characterized by a strong horizontal gradient of moisture with high values to the west (over the Mediterranean Sea) and low values to the east (over the Adriatic Sea). These conditions were propitious for the advection of moisture-laden warm air by the strong southerly flow associated with the trough, from the Mediterranean toward the southern slopes of the Alps. According to Rotunno and Ferretti (2001) this moist saturated airflow could cross over the Alps relatively easily because of its reduced effective static stability, while the drier air to the east was deflected by the Alps because of its stronger stability. This explains the origin of the easterly flow over the Po Valley, and hence the convergence in the Piedmont region. There are however noteworthy differences between the PF and the present case.

According to the Swiss Model analyses (Fig. 3) on 19 and 20 September 1999, no distinct horizontal gradient of moisture was observed in the environmental flow; the western part of the airstream was not significantly moister than the eastern part. On the contrary, at the time of maximum precipitation (0000 UTC 20 September, Fig. 3(b)) air was significantly drier over the Mediterranean than over the Adriatic. Data from radiosoundings launched at Ajaccio, Corsica (not shown), confirmed that the relative humidity was less than 30% up to 600–700 hPa during the precipitating period of IOP 2b. On the other hand, data from radiosoundings launched at Milano Linate (Figs. 4(a) and (c)) 40 km south-east of Lago Maggiore, and at Verona (Figs. 4(b) and (d)) about 140 km east of Lago Maggiore and 90 km west of the Adriatic coast,

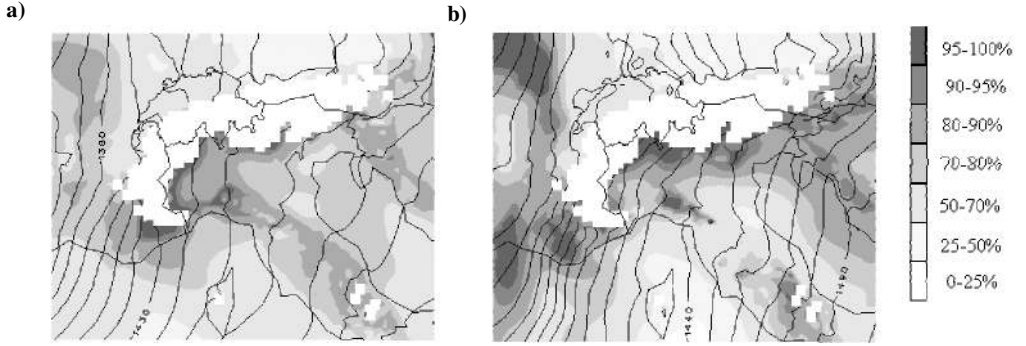
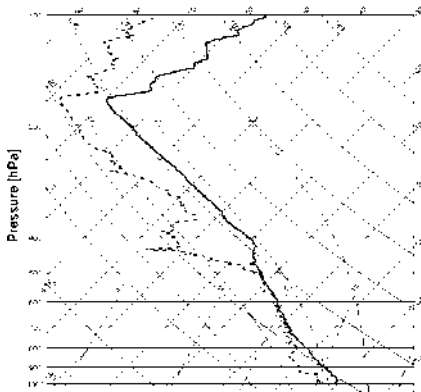
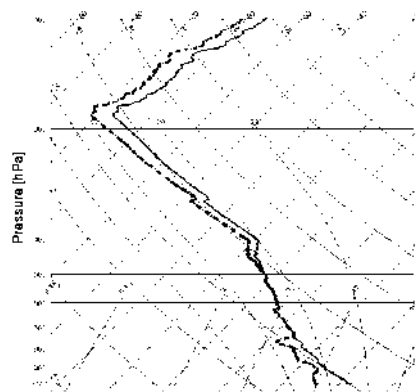


Figure 3. Swiss Model analysed relative humidity (grey-scale) and isohypses (contours every 10 m) at 850 hPa at: (a) 1200 UTC 19 September, (b) 0000 UTC 20 September. The white region encloses mountains above 850 hPa.

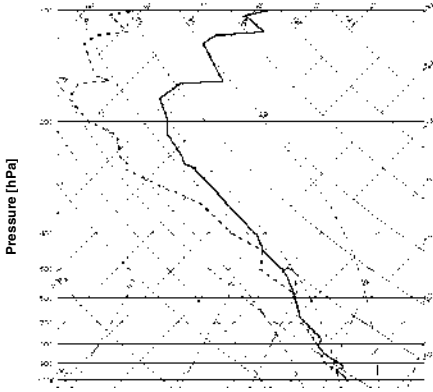
a) Milano/Linate



b) Verona



c) Milano/Linate



d) Verona

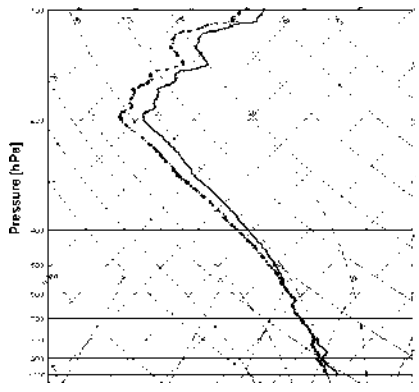


Figure 4. Skew T -Log p diagrams from radiosoundings launched at: (a) Milano-Linate, and (b) Verona at 1800 UTC 19 September 1999; (c) Milano-Linate, and (d) Verona at 1200 UTC 20 September 1999.

were very similar. From 1800 UTC 19 September until 1200 UTC 20 September, both stations reported the presence of very moist air below 500 hPa and moderate convective instability ($\leq 500 \text{ J kg}^{-1}$).

As can be deduced from the Milano-Linate radiosounding data at 1800 UTC 20 September (Fig. 4(a)), there was a separation of less than 500 m between the lifting condensation level and the level of free convection (LFC), located at 940 and 900 hPa, respectively, for an air parcel whose temperature and mixing ratio were averaged over the lowest 50 hPa. The energy per unit mass required to lift a negatively buoyant air parcel from the surface to the LFC (convective inhibition, CIN) was only 17 J kg^{-1} , indicating a weak low-level thermodynamic stability. The CAPE, i.e. the energy per unit mass that can be released through buoyancy from the LFC up to the equilibrium temperature level, here located at 180 hPa, was slightly less than 500 J kg^{-1} . During the afternoon and evening of 20 September, in association with the arrival of the cold front, the thermodynamic conditions changed remarkably: convective instability vanished due to cooling and drying in the low levels, and the tropopause descended from 150–200 hPa to about 300 hPa. This was consistent with the decreasing radar echoes over Lago Maggiore area after 1400 UTC 20 September, though some convective precipitation still occurred in the north-western Po Valley where cold post-frontal air passed over a small zone of secluded warm and moist air in the low levels.

It is therefore important to note that although IOP 2b and the PF presented similar dynamical characteristics—with convergence along the mountain barrier between the southerly flow from Mediterranean and the easterly flow from Adriatic—the thermodynamic characteristics of these convergent flows were different during these two events. Unlike the PF, during IOP 2b the southerly flow was not significantly moister than the south-easterly flow. Consequently, even if the easterly wind perturbations over the Po Valley resulted from the deflection of the eastern part of the airstream by the Alps in both cases, for IOP 2b it was not caused by stronger stability of air to the east but more probably by local orographic and large-scale dynamic effects.

3. RADAR OBSERVATIONS

(a) *Triple-Doppler radar network*

During MAP, three ground-based Doppler radar were operated in the Lago Maggiore area where, according to a precipitation climatology of the Alps from high-resolution rain-gauge observations by Frei and Schär (1998), prominent maxima of rainfall accumulation frequently occur. These were the Swiss Meteorological Agency operational Doppler radar at Monte-Lema (46.042°N , 8.833°E , 1625 m*), the US National Center for Atmospheric Research (NCAR) S-Pol polarimetric Doppler radar at the southern tip of Lago-Maggiore (45.720°N , 8.730°E , 280 m) near Vergiate, and the French Centre d'Etude des Environnements Terrestre et Planetaire (CETP) RONSARD Doppler radar near Novara at (45.460°N , 8.517°E , 155 m). The radar baseline was relatively wide, with a distance of about 75 km between RONSARD and Monte-Lema (S-Pol was located approximately midway between).

When the data from these three ground-based Doppler radars are combined, three-dimensional precipitation and wind fields can be retrieved from within a large domain with relatively high spatial and temporal resolutions. The horizontal domain shown in Fig. 5 is $150 \text{ km} \times 150 \text{ km}$ and is centred on 45.70°N , 8.60°E , approximately at the southern tip of the Lago Maggiore. This region encompasses very different terrain, with

* Heights are above mean sea level except where otherwise indicated.

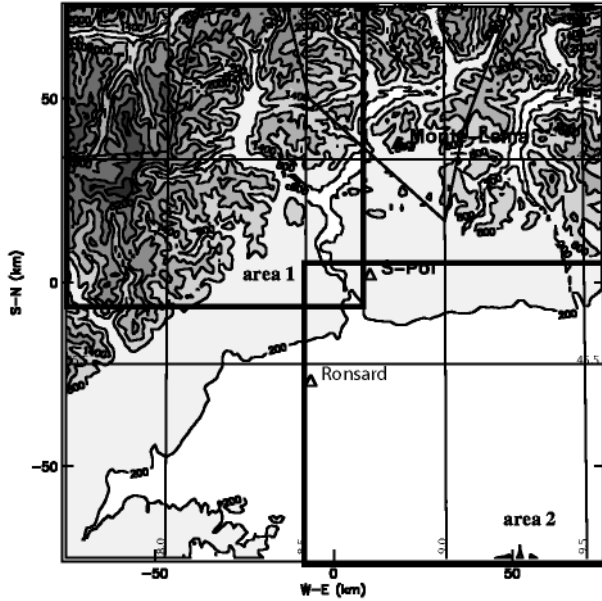


Figure 5. Triple-Doppler radar network and underlying terrain in the Lago Maggiore region during MAP (contours every 600 m).

the very flat Po Valley to the south, the hilly Piedmont to the south-west, the high Alpine peaks (with Monte-Rosa over 4000 m altitude) to the north-east with Lago Maggiore and the deep Toce and Ticino Valleys. Therefore, inhomogeneous precipitation and wind fields were expected over this large domain characterized by such variable topography. This led us to analyse radar observations in two distinct domains of $90 \text{ km} \times 90 \text{ km}$ (Fig. 5): area 1 in the north-west (centred on 46.00°N , 8.10°E) mainly covers the mountains; area 2 in the south-east (centred on 45.40°N , 9.00°E) mainly covers the plain.

(b) *Comparative evolution of precipitation and wind over the plain and the mountain*

Figure 6 shows a time series of mean wind and reflectivity profiles deduced from radar data from the three ground-based Doppler radars over areas 1 and 2. It is interesting to note that the structure of precipitation was more homogeneous over the mountains, with a moderate and quasi constant vertical development during the whole IOP, than over the plain where three convective periods could be distinguished with maximum reflectivity values at about 2300, 0400 and 1000 UTC. Nevertheless, a close inspection of the two series of reflectivity profiles reveals that precipitation observed over the southern flank of the Alps (area 1, Fig. 6(a)) depended on the situation prevailing over the Po Valley (area 2, Fig. 6(b)) about one hour before. For instance, the persistent precipitation observed over the mountainous area from 2000 UTC 19 September till 0130 UTC 20 September with a reflectivity maximum at 0000 UTC, can be related to the rain event over the plain from 1900 UTC 19 September till 0030 UTC 20 September with a reflectivity maximum at 2300 UTC. Likewise, the third convective event observed over the plain, characterized by an increase of reflectivity from 0800 till 1000 UTC on 20 September, can be related to the enhancement of precipitation occurring over the mountainous area approximately one hour later. Despite a comparable duration, the second major rain event observed over the plain from 0200 till 0830 UTC apparently did

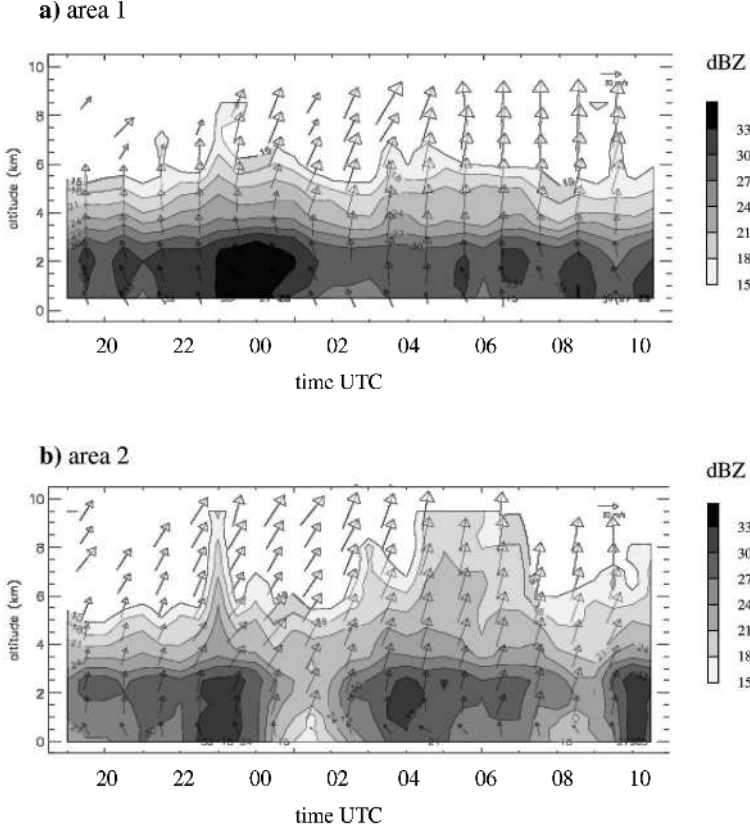


Figure 6. Mean reflectivity profiles (contours every 3 dBZ) and superimposed mean horizontal wind vector (reference vector in upper-right corner) evolution from 1900 UTC 19 September to 1030 UTC 20 September 1999: (a) over the mountains (area 1), (b) over the plain (area 2).

not influence orographic precipitation as strongly as the first event, even if there was a slight increase of reflectivity over the mountains from 0300 till 0730 UTC.

Vertical profiles of the mean horizontal wind in areas 1 and 2 are also shown in Fig. 6. For each area and each level, z , the mean wind components U_0 and V_0 have been deduced from the Doppler velocity, V_D , values, corrected for the reflectivity-derived fall speed V_F , through the minimization of cost-functions $J_{UV}(z)$ defined as:

$$J_{UV}(z) = \iiint_D \{ (V_D - V_F \sin \beta) - (U_0 + U_X X + U_Y Y) \cos \alpha \cos \beta - (V_0 + V_X X + V_Y Y) \sin \alpha \cos \beta \}^2 dx dy dz,$$

where $D(z)$ is a three-dimensional domain of $90 \text{ km} \times 90 \text{ km} \times 0.5 \text{ km}$ for each of areas 1 and 2, centred on the considered altitude; α and β are the radar-relative azimuth (counter-clockwise from the east) and elevation, respectively; X and Y are eastward and northward Cartesian coordinates with their origin at the centre of the considered areas; U_X , U_Y , V_X , V_Y are the first-order wind derivatives. In Fig. 6, we identify the southerly and westerly wind components by showing the horizontal wind vector as a function of altitude and time. The persistent south-easterly flow in the low levels favoured the propagation of convective cells from the Po Valley toward the Alps in a

direction almost perpendicular to the mountain range in the considered domain, leading to the development of precipitation over the windward slopes of the mountains (Medina and Houze 2003, Figs. 10(b) and 11(a)). This could explain the continuous precipitation over the orography as well as the delay between the observed reflectivity maxima over the plain and the mountainous area.

The mean south-easterly flow below 1 km progressively veered to south and south-west aloft, especially between 0100 and 0400 UTC over the mountains (Fig. 6(a)) and between 0000 and 0300 UTC over the plain (Fig. 6(b)), which corresponded to the period of less intense precipitation. This clockwise turn with altitude was more marked over the plain where the flow became predominantly south-westerly above 1.5 km during this period. This south-westerly flow was not favourable for the development of precipitation either over the plain or over the mountains (Houze *et al.* 2001) despite an enhancement of wind intensity at all levels. Two main reasons for that were: (i) this flow was characterized by low moisture (see section 2(b)); (ii) the low-level wind was then less perpendicular to the mountain range.

(c) *Three-dimensional analysis of precipitation and wind fields*

Three-dimensional wind and reflectivity fields have been deduced from triple-Doppler data using the real-time and automated multiple-Doppler analysis method (RAMDAM, Chong *et al.* 2000). A similar version of RAMDAM was used in the Project Operation Centre with low-resolution radar data for display purposes and guidance of the instrumented aircraft operations during the SOP. The grid resolution here is 2 km in the horizontal and 0.5 km in the vertical, and the horizontal domain is 150 km \times 150 km (see Fig. 5). Figure 7 shows the evolution (every two hours between 2000 and 2400 UTC on 19 September) of the horizontal wind and reflectivity at 2.5 km altitude. This period corresponded to the first major convective event observed over flat terrain (see Fig. 6). Figure 8 concerns the period from 0200 till 0600 UTC 20 September during which the second major rain event occurred, but the horizontal cross-sections are now at 2 km altitude in order to take into account the slightly lower altitude of the reflectivity contours over the mountains after 0100 UTC (see Fig. 6(a)).

During the period including the two major rain events over the Po Valley, evolutions of the easterly component of the wind (negative values in Figs. 7(b), (d) and (f), and Figs. 8(b), (d) and (f)) and of the reflectivity patterns were fairly well correlated; both followed a similar enhancement–attenuation cycle over the considered domain. In particular, the strongest precipitation occurred where and when the easterly wind component was the largest with, however, a preferred and persistent location on the southern flank of the Alps. The only exception concerned the south-eastern flat part of the domain at 0600 UTC (Fig. 8) where relatively strong precipitation occurred despite a westerly wind. This could, however, be a remnant of the rain event observed at the same location two hours before, in association with the easterly perturbation.

Even if it was moderate, the easterly wind component seemed essential to trigger precipitation as previously observed in section 3(b). As supposed by Ferretti *et al.* (2000), unstable air lifted by the ‘rotated-L’ shape of the western Alps can produce PV through latent-heat induced vortex stretching. Then, the associated easterly wind perturbations towards the concave western part of the rotated-L corresponding to the Piedmont region would enhance horizontal convergence in the low levels and favour further lifting of unstable air. But, Rotunno and Ferretti (2001) showed that this phenomenon was not essential for intense rainfall in the Po Valley during the PF, which could rather be related to the blocking and deflection of unsaturated air coming from the east of the Alpine barrier. In the present case, this explanation can hardly explain the presence of

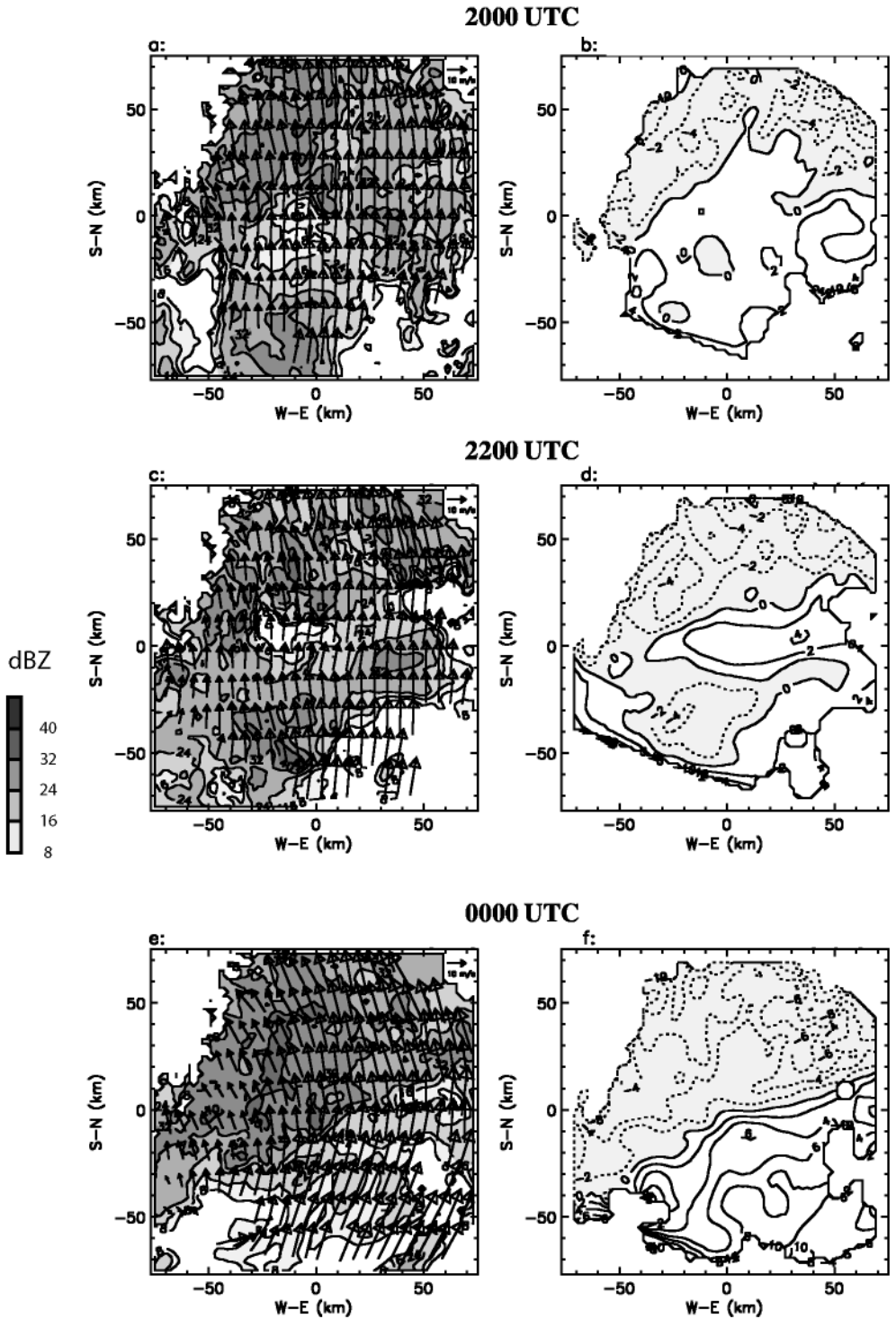


Figure 7. Horizontal cross-section in the Lago Maggiore region at 2.5 km altitude of: (a) wind vectors (reference vector in upper-right corner) with superimposed radar reflectivity values (contours every 8 dBZ), and (b) zonal wind component (contours every 2 m s^{-1}), at 2000 UTC 19 September 1999; (c) and (d) as (a) and (b), respectively, but for 2200 UTC; (e) and (f) as (a) and (b), respectively, but for 0000 UTC 20 September 1999.

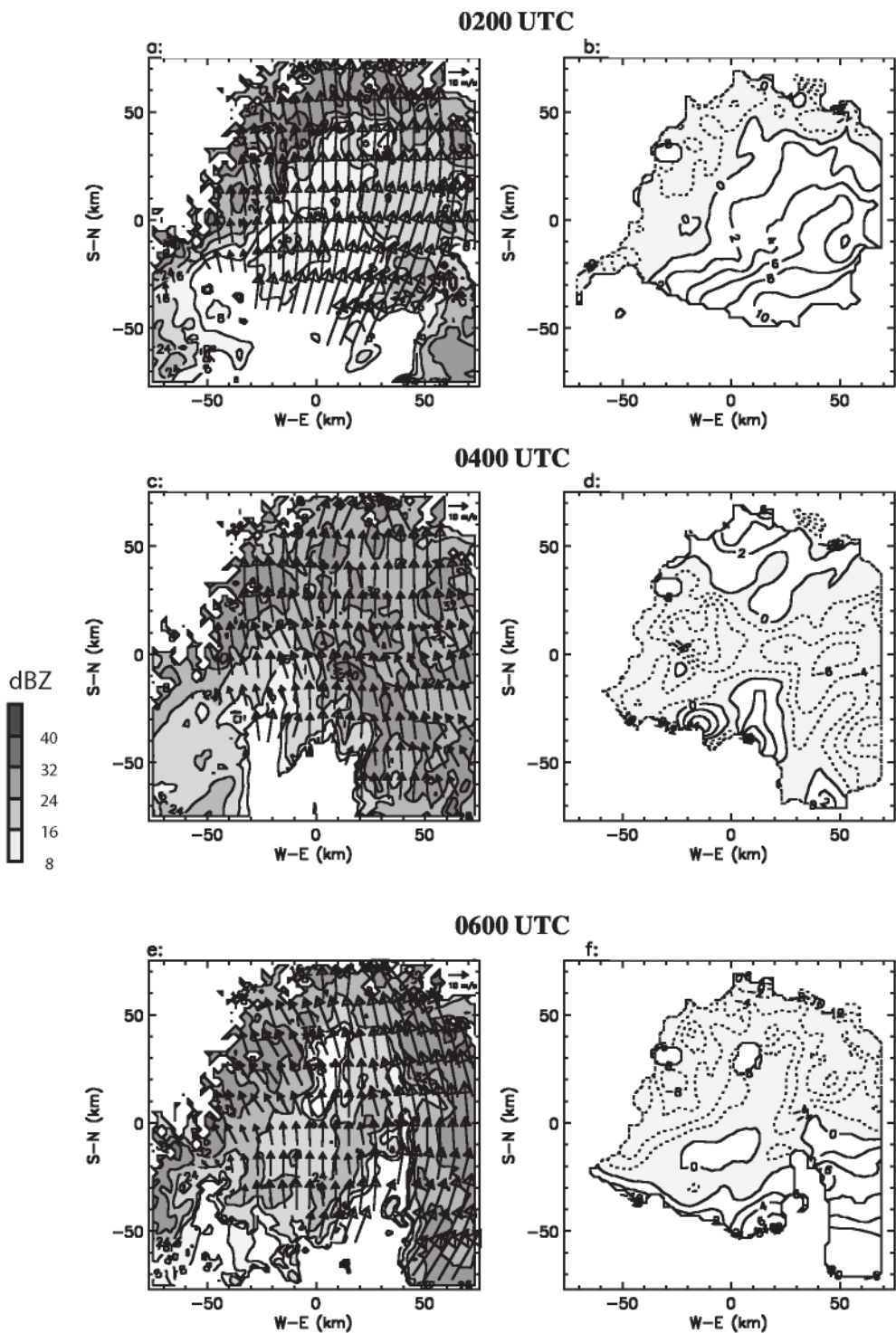


Figure 8. As Fig. 7, except at 2 km altitude, and with (a) and (b) at 0200 UTC, (c) and (d) at 0400 UTC, and (e) and (f) at 0600 UTC 20 September 1999.

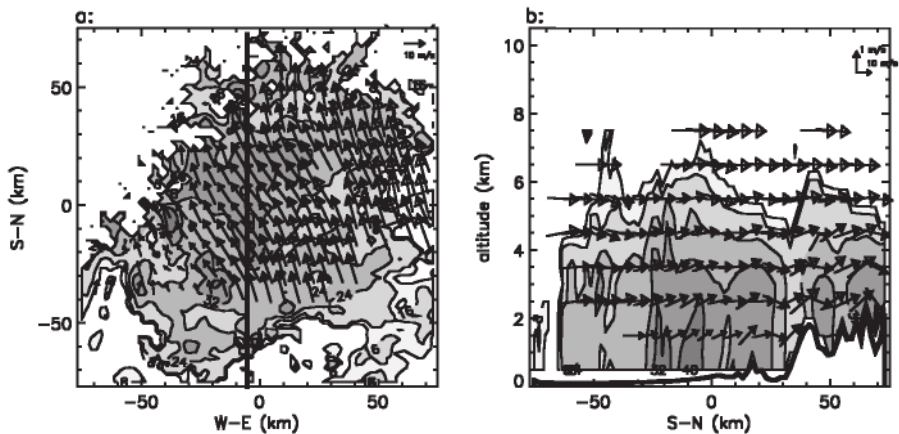


Figure 9. Wind vectors (reference vectors in upper-right corners) and reflectivity (contours every 8 dBZ, starting at 8 dBZ) in the Lago Maggiore region at 2300 UTC 19 September 1999 for: (a) a horizontal cross-section at 1.5 km altitude, and (b) a vertical cross-section at $X = -5$ km, as shown by the bold line in (a).

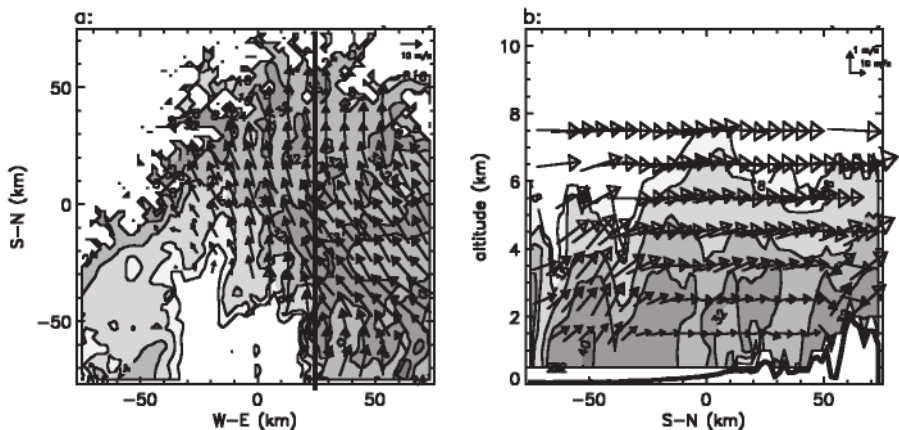


Figure 10. As Fig. 9, except at 0400 UTC 20 September 1999, and (b) is at $X = +27$ km.

easterly winds over the plain but not over the mountains (e.g. Fig. 8(d)). Furthermore, an important difference from the PF is the rather high humidity over the eastern Po Valley during IOP 2b (see Fig. 4). Hence, we suggest that in addition to the westward deflection of the southerly flow toward the mountains, the sporadic enhancement of the moist flow coming from the Adriatic Sea could also be involved as one of the main factors for the generation of heavy precipitation in the Lago Maggiore region during IOP 2b.

Further information on the organization of precipitation during IOP 2b can be deduced from the reflectivity and wind fields. In particular, the influence of orography was significant since precipitation remained almost stationary over the southern flank of the Alps with a mean reflectivity of around 30 dBZ and maxima of up to 50 dBZ, while over the southern flat part of the domain more or less intense cells alternated with stratiform echoes or no precipitation at all. During the first convective event observed over the plain, convective cells formed over the Po Valley in the southern part of the

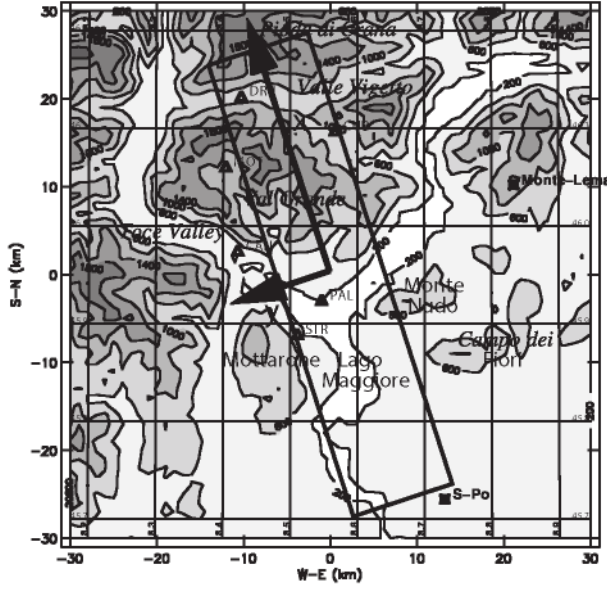


Figure 11. Sub-domain of the Lago Maggiore region where high-resolution wind and reflectivity fields were obtained. Locations of the radars and of the surface stations (STRESA, PALANZA, CANDOGlia, CURSOLA, MOTTA, DRUOGNO) are indicated. Major topographic features are labelled (contours every 200 m). Domain D and axes x and y for the two-dimensional analyses are indicated.

considered domain and propagated northwards toward the mountains (Figs. 7(a), (c) and (e)). These cells then merged with the older ones over the windward slopes of the Alps north-west of Lago Maggiore where the strongest reflectivity values were observed.

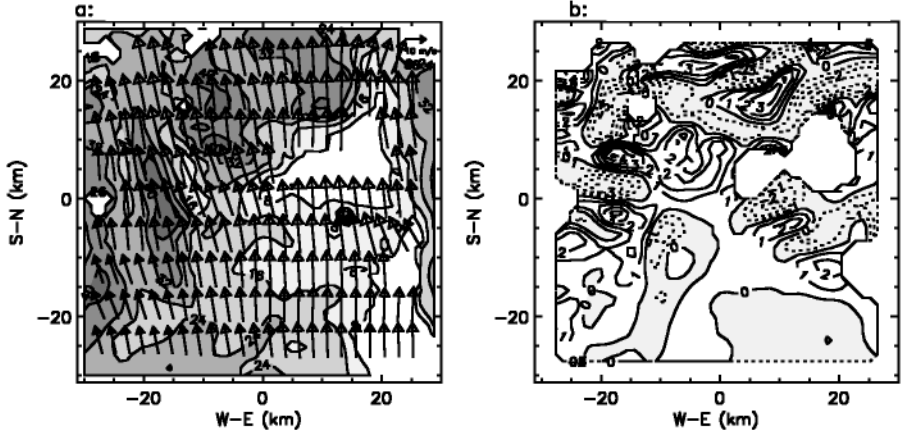
The second convective event observed over the Po Valley (from 0300 to 0700 UTC 20 September) began in the eastern part of the domain and spread progressively westwards under the influence of the well-marked easterly flow (Figs. 8(a), (c) and (e)). As shown in Fig. 8(c), the maximum convective activity over the plain at 0400 UTC corresponded to the maximum convergence between the predominantly southerly flow and the intensifying easterly flow. Such a convergence was not observed during the first convective event (Fig. 7).

Figures 9 and 10 show wind and reflectivity in south–north vertical cross-sections through the most intense precipitation zones. As expected, because of a strong convergence in the horizontal wind, the vertical velocities associated with the highest reflectivity were significantly stronger at 0400 than at 2300 UTC. In particular, upward motions occurred about 100 km upstream of the Alpine barrier (Fig. 10(b)) where orographic forcing does not exist. However, the low-level flow was less intense during this second period (see also Fig. 6). Such conditions were more favourable to local development of precipitation over the plain where convergence occurred, but made the transport of cells from the Po Valley toward the Alps less efficient than at 2300 UTC. This could explain why the second intense rain episode over the plain had a weaker influence on precipitation over the mountains.

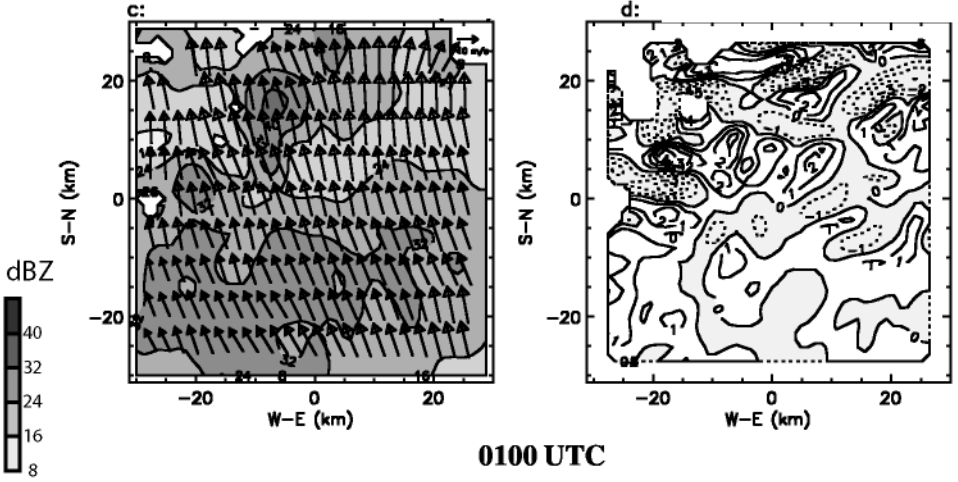
(d) Local orographic effects on the kinematics and precipitation field

In order to better emphasize the influence of orographic effects on rainfall location and intensity, three-dimensional wind and precipitation fields at higher horizontal

2100 UTC



2300 UTC



0100 UTC

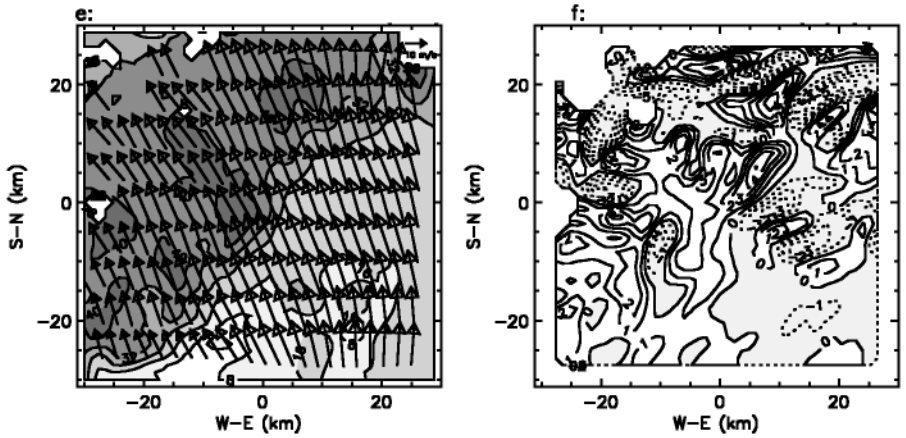


Figure 12. Horizontal cross-sections, in a sub-domain of the Lago Maggiore region, at 2 km altitude of: (a) wind vectors (reference vector in upper-right corner) with superimposed radar reflectivity values (contours every 8 dBZ), and (b) vertical wind component (contours every 1 m s^{-1} , shaded zones denote downward motions) at 2100 UTC 19 September 1999; (c) and (d) as (a) and (b), respectively, but for 2300 UTC; (e) and (f) as (a) and (b), respectively, but for 0100 UTC 20 September 1999.

resolution (1.2 km) have been derived from the multi-Doppler data in a domain of 60 km \times 60 km centred on the Lago Maggiore at 45.95°N, 8.56°E (Fig. 11). This is the region where precipitation was most intense and persistent. Figure 12 shows the horizontal wind field with the associated vertical velocity and reflectivity values at 2100 and 2300 UTC 19 September and 0100 UTC 20 September, during the first and most intense rainfall event. Two distinct regimes of orographic flow corresponded to two types of rainfall distribution and intensity. The first one (from 2100 till 2300 UTC) was characterized by a horizontal flow of about 15–17 m s⁻¹ at 2 km altitude which was strongly affected by the underlying terrain. Note for example the systematic deflection of the flow at $[X = -10 \text{ km}, Y = 0 \text{ km}]$ and $[X = +20 \text{ km}, Y = +20 \text{ km}]$ which probably corresponded to air channelling in the Toce and Ticino Valleys because of the presence of Monte Grande and Pioda di Crana massifs north of the Lago Maggiore (Fig. 11) with peaks over 2000 m.

The second regime (at 0100 UTC, Figs. 12(e) and (f)) was characterized by a stronger horizontal south-easterly flow (up to 24 m s⁻¹ at 2 km altitude) which was less perturbed by the orography. This caused a more efficient advection of cells from the Po Valley toward the Alps, along a direction almost perpendicular to the mean orientation of the mountain range. This led to a more uniformly distributed rainfall over the mountains. For both regimes, vertical velocities were strongly related to the underlying terrain, with the strongest upward motions over the windward slopes and the strongest downward motions over the leeward slopes. As a consequence, the most intense rainfall occurred where and when the flow impinging on the mountains was a maximum.

4. TWO-DIMENSIONAL WATER BUDGET

(a) *Two-dimensional wind and reflectivity fields*

In order to quantify the relations between orographic forcing and northward advection of rain cells from the Po Valley in the generation of precipitation over the mountainous region north of Lago Maggiore, a series of 25 vertical cross-sections of wind and reflectivity fields has been derived between 2000 UTC 19 September and 0200 UTC 20 September. These are along a direction parallel to the density-weighted mean wind below 6 km altitude, and are taken from the ‘high-resolution’ multiple-Doppler analyses discussed above, with the same horizontal (1.2 km) and vertical (0.5 km) grid spacings. As seen in Fig. 11, from south-east to north-west the considered domain D (54 km long, 12 km wide, 9 km deep) encompasses the relatively flat terrain at 200–250 m altitude near the southern part of Lago Maggiore (between Mottarone on the western bank and Campo dei Fiori and Monte Nudo on the eastern bank), the relatively steep upward slope of Val Grande massif with peaks over 2000 m, then Valle Vigetto at 600–700 m, and the upward slope of Pioda di Crana. This domain was chosen for two reasons: firstly, it is the only one showing a relatively homogeneous topography in the direction normal to the mean wind direction; secondly, it was well observed by the S-Pol radar (RONSARD and Monte-Lema have a slightly lower spatial resolution here).

Since our goal is to quantify the contributions of sources and fluxes in the water budget, it is necessary to ensure mass balance and compatibility for the series of wind fields. Hence, the two-dimensional wind fields must obey two constraints: (i) to be as close as possible to the radar-derived winds; (ii) to verify the two-dimensional air mass continuity equation with a lower boundary given by the mean topography $h_{2D}(x)$, where x is the axis oriented 162–342° (see Fig. 11). This is obtained through the minimization

of cost-function J_Ψ , defined as:

$$J_\Psi = \iiint_D \left[\left\{ \frac{\partial \Psi(x, z)}{\partial x} - \rho(z)u(x, y, z) \right\}^2 + \left\{ \frac{\partial \Psi(x, z)}{\partial z} + \rho(z)w(x, y, z) \right\}^2 \right] dx dy dz + \int_{x=-27 \text{ km}}^{x=+27 \text{ km}} \left[\frac{\partial \Psi\{x, h(x)\}}{\partial x} - \frac{\partial h_{2D}(x)}{\partial x} \frac{\partial \Psi\{x, h(x)\}}{\partial z} \right]^2 dx,$$

with

$$h_{2D}(x) = \frac{1}{12 \text{ km}} \int_{y=-6 \text{ km}}^{y=+6 \text{ km}} h(x, y) dy,$$

where $\Psi(x, z)$ is a two-dimensional stream function, y the direction ($252-72^\circ$) normal to x (see Fig. 11), z is the vertical coordinate, ρ is the air density, and u and w are the radar-derived wind components. The two-dimensional wind components, u_{2D} and w_{2D} , are then obtained through:

$$\frac{\partial J_\Psi}{\partial \Psi(x, z)} = 0 \quad \text{for } (x, z) \in D; \quad u_{2D}(x, z) = + \frac{1}{\rho(z)} \frac{\partial \Psi(x, z)}{\partial z};$$

$$w_{2D}(x, z) = - \frac{1}{\rho(z)} \frac{\partial \Psi(x, z)}{\partial x}.$$

We have verified for the 25 sequences from 2000 UTC on 19 September till 0200 UTC on 20 September that: (i) the horizontal wind divergence along x was much larger than along y (r.m.s. $(\partial u / \partial x) = 1.2$ to $2.2 \times 10^{-3} \text{ s}^{-1} >$ r.m.s. $(\partial v / \partial y) = 0.07$ to $0.16 \times 10^{-3} \text{ s}^{-1}$); (ii) the strongest orographic forcing occurred along x (r.m.s. $(u \times \partial h(x, y) / \partial x) = 0.35$ to $0.55 \text{ m s}^{-1} <$ r.m.s. $(v \times \partial h(x, y) / \partial y) = 0.02$ to 0.07 m s^{-1}); (iii) the two-dimensional velocities were close to the radar-derived ones (r.m.s. $(u_{2D} - u) / \text{r.m.s.}(u) = 0.06$ to 0.13 ; r.m.s. $(w_{2D} - w) / \text{r.m.s.}(w) = 0.21$ to 0.46).

Since the upper limit of the domain where radar data were available changed with time, a common upper boundary must be set to obtain homogeneous results from the series of 25 sequences. As shown in Fig. 13, this upper limit, $z_{\text{top}}(x)$, was chosen as that defined by the streamline entering the domain at $x = -27 \text{ km}$ and 5 km altitude. The height of this upper limit within the domain ($-27 < x < +27 \text{ km}$) depended on the horizontal and vertical motions for the considered sequence. It is also to be noted that the mass flux between the surface level and this upper limit was strictly constant with x for a given sequence, but varied with time since it depended on the intensity of the horizontal inflow below 5 km altitude at $x = -27 \text{ km}$.

(b) Radar- and gauge-derived rain rates

Rainfall rates are derived from the three-dimensional reflectivity values using the relation:

$$Z(\text{mm}^6 \text{m}^{-3}) = A (R(\text{mm h}^{-1}))^B$$

where coefficients A and B for rain ($T > 0^\circ \text{C}$: $A = 265$, $B = 1.45$) are intermediate values between those classically used for convective (Sekhon and Srivastava 1971) and stratiform (Marshall and Palmer 1948) precipitation; for ice ($T < -10^\circ \text{C}$) we take $A = 1780$, $B = 2.21$ (Sekhon and Srivastava 1970), and the values are interpolated for intermediate air temperatures ($-10 < T < 0^\circ \text{C}$).

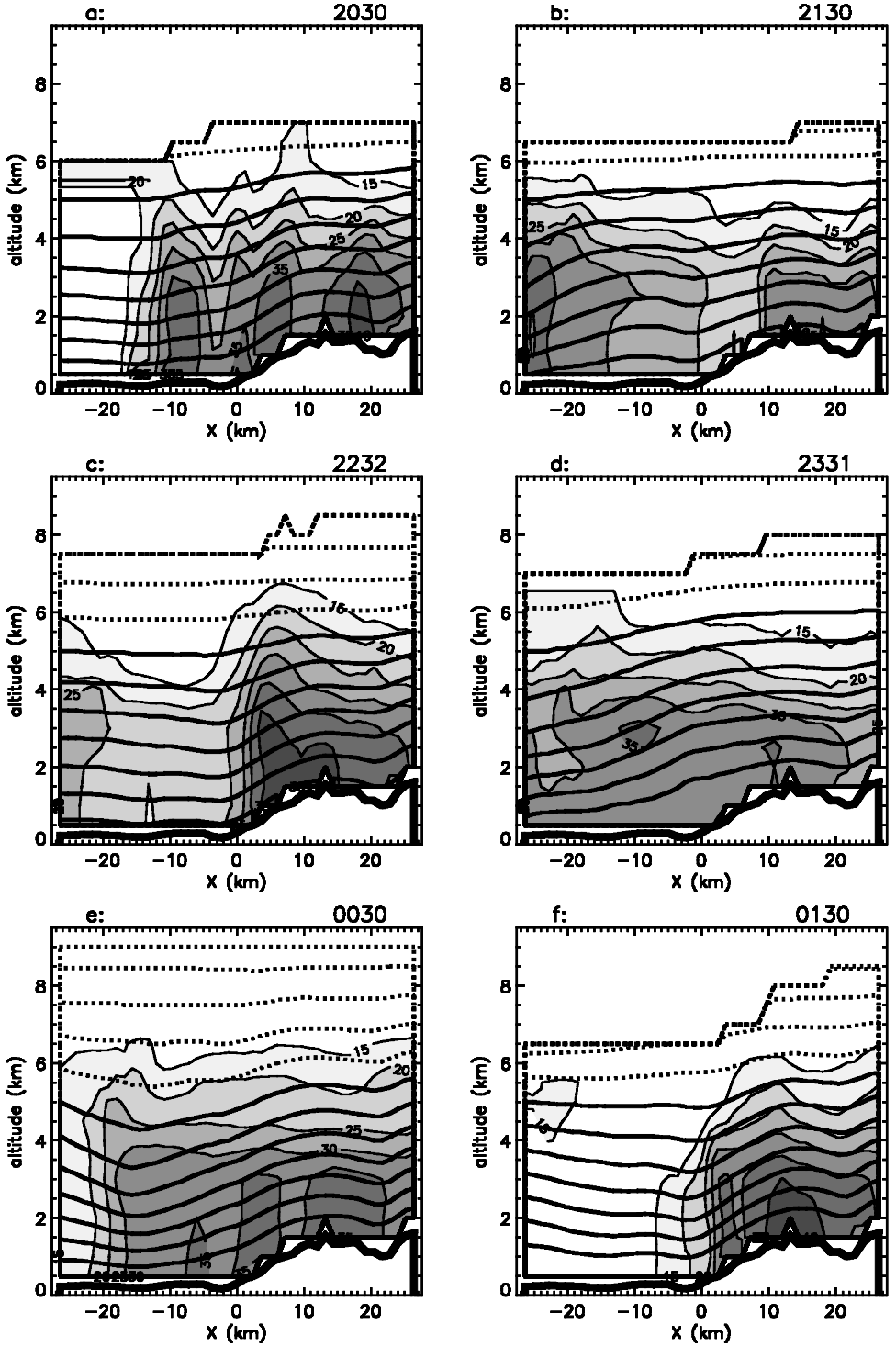


Figure 13. Stream function (isolines, contours every $10^4 \text{ kg m}^{-1} \text{ s}^{-1}$, dashed lines for inflow above 5 km altitude), and mean reflectivity values (grey shading, contours every 5 dBZ) in the two-dimensional vertical cross section along x (see text) for: (a) 2030 UTC, (b) 2130 UTC, (c) 2232 UTC, and (d) 2331 UTC 19 September 1999; (e) 0030 UTC, and (f) 0130 UTC 20 September 1999. The thick solid line denotes the mean surface altitude $h_{2D}(x)$.

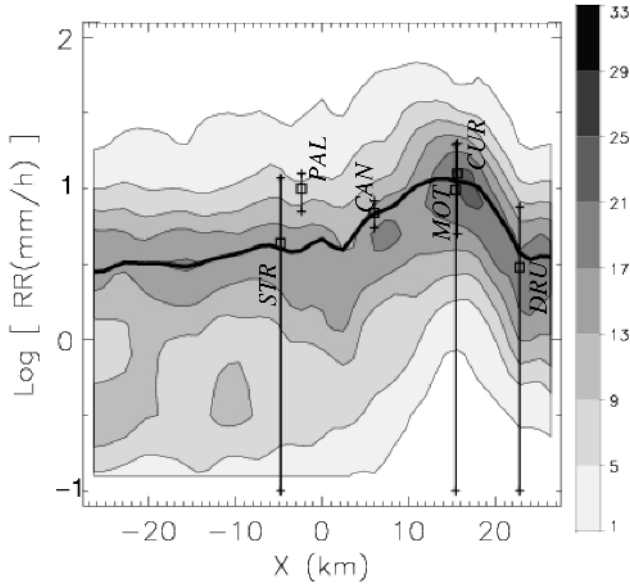


Figure 14. Contoured frequency display of radar-derived rainfall rate (contours every 4% of occurrence) along x (see text). The solid line represents the mean value. Mean rain rates and standard deviations from the six surface stations (locations given in Fig. 11) are also indicated.

It is well known that there is substantial variability in relations between Z and R from rain event to rain event, as well as within a single event (e.g. Austin 1987). For this reason, and others related to classical problems with radar measurements of precipitation (radar calibration, beam blockage, anomalous propagation, attenuation by precipitation, range effects, non-uniform beam filling, variation in precipitation with height, etc.), there is some unquantifiable uncertainty in the two-dimensional radar-derived precipitation amounts and rates. It is therefore necessary to check them against independent values from rain-gauges. However, rain-gauge measurements are not error free owing to local characteristics of topography, limited sampling surface, mechanical problems, wind and turbulence effects, etc. Hence, instead of point-to-point comparisons, it seems more appropriate to compare the frequency distributions of radar- and gauge-derived precipitation rates.

The frequency distribution of reflectivity-derived rain rates along x is displayed in Fig. 14 through a ‘contoured frequency display’. This is basically similar to the ‘Contoured Frequency by Altitude Display’, or CFAD, used by Yuter and Houze (1995) to visualize a variation of the statistical distribution of various quantities with respect to altitude, except that here Fig. 14 shows a variation with respect to x . For each point along x , variability with respect to both perpendicular direction ($-6 < y < +6$ km in Fig. 11) and time (25 sequences from 2000 to 0200 UTC) has been taken into account. On the same diagram, mean rain rates and their standard deviations measured during the same period at six nearby surface stations (locations given in Fig. 11) are plotted as functions of their equivalent location along x . Except for Pallanza, very good agreement is found between the mean radar- and gauge-derived rain rates, with values increasing from 2.8 mm h^{-1} at $x = -27 \text{ km}$ to 4.3 mm h^{-1} at $x = +2 \text{ km}$ over the flat terrain, a strong increase up to 12.3 mm h^{-1} at $x = +14 \text{ km}$ over the first mountain top (Val Grande), and a large decrease down to 3.3 mm h^{-1} at $x = +25 \text{ km}$ in Valle Vigetto. Houze and

Medina (2001) and Medina and Houze (2003) have also shown from the S-Pol radar data alone that the maximum precipitation occurred over the first major peak of terrain in this storm. Except for the very low rain rates sporadically observed at Mottac and Druogno, the gauge-derived variability agrees with the radar-derived variability, with different characteristics of the radar-derived rainfall rates over the plain (two orders of magnitude) and the mountain (one-and-a-half orders of magnitude). This result is similar to that obtained by Germann and Joss (2001) who found that, over a somewhat larger zone encompassing Lago Maggiore and for 96 h of September 1999 rain, the precipitation amount is relatively small and its variation is moderate over the plain, while the rain amount is moderate to high and its variation is weak over the mountains.

(c) Water budget equations

When the atmospheric water content is separated into three categories, water vapour q_v , non-precipitating cloud q_c , and precipitation q_p (no distinction is made between liquid water and ice), three conservation equations can be written:

$$\frac{\partial \rho q_v}{\partial t} + \nabla(\rho q_v \mathbf{V}) - F_{q_v} = -k + e, \quad (1)$$

$$\frac{\partial \rho q_c}{\partial t} + \nabla(\rho q_c \mathbf{V}) - F_{q_c} = +k - c, \quad (2)$$

$$\frac{\partial \rho q_p}{\partial t} + \nabla(\rho q_p \mathbf{V}) + \frac{\partial}{\partial z}(\rho q_p v_p) - F_{q_p} = p(q_p) = +c - e, \quad (3)$$

where \mathbf{V} is the air velocity, q_p is the precipitation content and v_p is the precipitation fall speed (we use $v_p = 3.32 Z^{0.06}(\rho_0/\rho)^{0.4}$ for $T > 0^\circ\text{C}$, $v_p = 0.69 Z^{0.06}(\rho_0/\rho)^{0.4}$ for $T < -10^\circ\text{C}$, and a linear interpolation for $-10 < T < 0^\circ\text{C}$), k is the ‘condensation’ rate ($q_v \rightarrow q_c$), e is the ‘evaporation’ rate ($q_p \rightarrow q_v$), c is the ‘conversion’ rate ($q_c \rightarrow q_p$), and F_{q_i} is the turbulent dissipation rate of quantity q_i .

The left-hand side of (3), the ‘production rate of precipitation’ $p(q_p)$, can be estimated from the radar-derived two-dimensional wind and reflectivity fields. The condensation rate k can be deduced from retrieved virtual-cloud potential-temperature perturbations θ_{c1} (not shown, see Roux *et al.* 1993 for details) as:

$$k = -\frac{C_p \pi_0}{L} \left\{ \frac{\partial \theta_{c1}}{\partial t} + (\mathbf{V} \cdot \nabla) \theta_{c1} \right\},$$

where π_0 is the environmental non-dimensional pressure (Exner function), C_p is the specific heat of air at constant pressure, L is the latent-heat of vaporization or sublimation (depending on T). The reason for using retrieved temperature perturbations to estimate k , instead of a simpler parametrization such as $w \times (dq_A/dz - dq_0/dz)$ (where dq_A/dz and dq_0/dz are the pseudo-adiabatic and environmental vertical gradients of humidity derived from radiosounding data), is that the associated condensational heating or evaporative cooling rates are those representing a best fit between the thermodynamic environment and the two-dimensional wind and reflectivity fields, in terms of agreement with the momentum and thermodynamic equations. Terms c and e in (3) can be deduced from the estimated k and $p(q_p)$ as:

- if $k < 0$ (i.e. saturated air) and $p(q_p) > 0 \quad \rightarrow \quad c = p(q_p), e = 0;$
- if $k > 0$ (i.e. unsaturated air) and $p(q_p) < 0 \quad \rightarrow \quad c = 0, e = \{k - p(q_p)\}/2;$
- otherwise $\rightarrow \quad k = 0, c = 0, e = 0.$

In order to study the atmospheric water budget, (1), (2) and (3) are integrated for each of the 25 successive analyses over the two-dimensional domain with the following lateral boundaries:

- lower boundary: $-27 \leq x \leq +27$ km, $z = h(x)$;
- upper boundary: $-27 \leq x \leq +27$ km, $z = z_{\text{top}}(x)$;
- south-eastern (inflow) boundary: $x = -27$ km, $h(-27 \text{ km}) \leq z \leq 5$ km;
- north-western (outflow) boundary: $x = +27$ km, $h(+27 \text{ km}) \leq z \leq z_{\text{top}}(+27 \text{ km})$;

where $z_{\text{top}}(x)$ for $-27 < x < +27$ km is determined by mass conservation (see Fig. 13). Supposing that time evolution and turbulent diffusion can be neglected, the integral forms of (1), (2) and (3) may be written as:

$$-FQV_{\text{in}} + FQV_{\text{out}} = -K + E, \quad (4)$$

$$-FQC_{\text{in}} + FQC_{\text{out}} = +K - C, \quad (5)$$

$$-FQP_{\text{in}} - FQP_{\text{top}} + FQP_{\text{sfc}} + FQP_{\text{out}} = +C - E, \quad (6)$$

where FQI_{in} and FQI_{out} denote the inflow and outflow of quantity q_i through the lateral boundaries at $x = -27$ and $x = +27$ km, respectively; FQP_{top} and FQP_{sfc} are the precipitation fluxes through the top and bottom boundaries (water vapour and cloud follow the streamlines, so these terms cancel for q_v and q_c); K , E and C are the two-dimensional integrals of k , e and c . Since no information is available on the moisture and cloud content of the air entering the considered domain (at $x = -27$ km), we will suppose that FQV_{in} in (4) can be estimated using the humidity profile from Milano-Linate radiosounding at 0000 UTC 20 September, and FQC_{in} will be set to zero. With these approximations, the remaining unknown terms FQV_{out} and FQC_{out} can be calculated.

We first verified the consistency between the left- and right-hand sides of (6). Since the conversion rate, C , and evaporation rate, E , are derived from two independent estimates, k and $p(q_p)$, such a balance is not implicit. We found that the r.m.s. values of $(-FQP_{\text{in}} - FQP_{\text{top}} + FQP_{\text{sfc}} + FQP_{\text{out}})$ and $(+C - E)$ are 81.2 and 74.3 kg m⁻¹s⁻¹, respectively, with a standard deviation of 15.4 kg m⁻¹s⁻¹ between these two terms. This last value can be considered as an estimate of the uncertainty in the water budget.

(d) Characteristics of the water budget

Figure 15 shows the evolution of the various integral quantities between 2000 and 0200 UTC. The moisture inflow FQV_{in} (Fig. 15(a)) displays substantial variations during this period with three maxima at 2000 (523 kg m⁻¹s⁻¹), 2145 (503 kg m⁻¹s⁻¹) and 0045 UTC (583 kg m⁻¹s⁻¹), and three minima at 2100 (472 kg m⁻¹s⁻¹), 2235 (464 kg m⁻¹s⁻¹) and 0145 UTC (499 kg m⁻¹s⁻¹). Since the humidity profile is kept constant at inflow, these variations are related to changes in the intensity of the horizontal wind. The flows of precipitation through the lateral boundaries (FQP_{in} and FQP_{out}) and the top of the domain (FQP_{top}), as well as the evaporation rate (not shown) are much smaller (0.4 to 14 kg m⁻¹s⁻¹). The integrated rates of condensation K (Fig. 15(b)), conversion C (Fig. 15(c)) and surface precipitation FQP_{sfc} (Fig. 15(d)) have intermediate values. A noteworthy characteristic is the time shift between condensation (with maxima of 91 kg m⁻¹s⁻¹ at 2015, 90 kg m⁻¹s⁻¹ at 2215, 103 kg m⁻¹s⁻¹ at 2345, and 108 kg m⁻¹s⁻¹ at 0045 UTC) and surface precipitation (with maxima of 83 kg m⁻¹s⁻¹—or 5.5 mm h⁻¹ when uniformly distributed from $x = -27$ to $+27$ km—at 2030, 99 kg m⁻¹s⁻¹ or 6.6 mm h⁻¹ at 2230, and 102 kg m⁻¹s⁻¹ or 6.8 mm h⁻¹ at 0115 UTC). Conversion rates display maxima at more or less intermediate times.

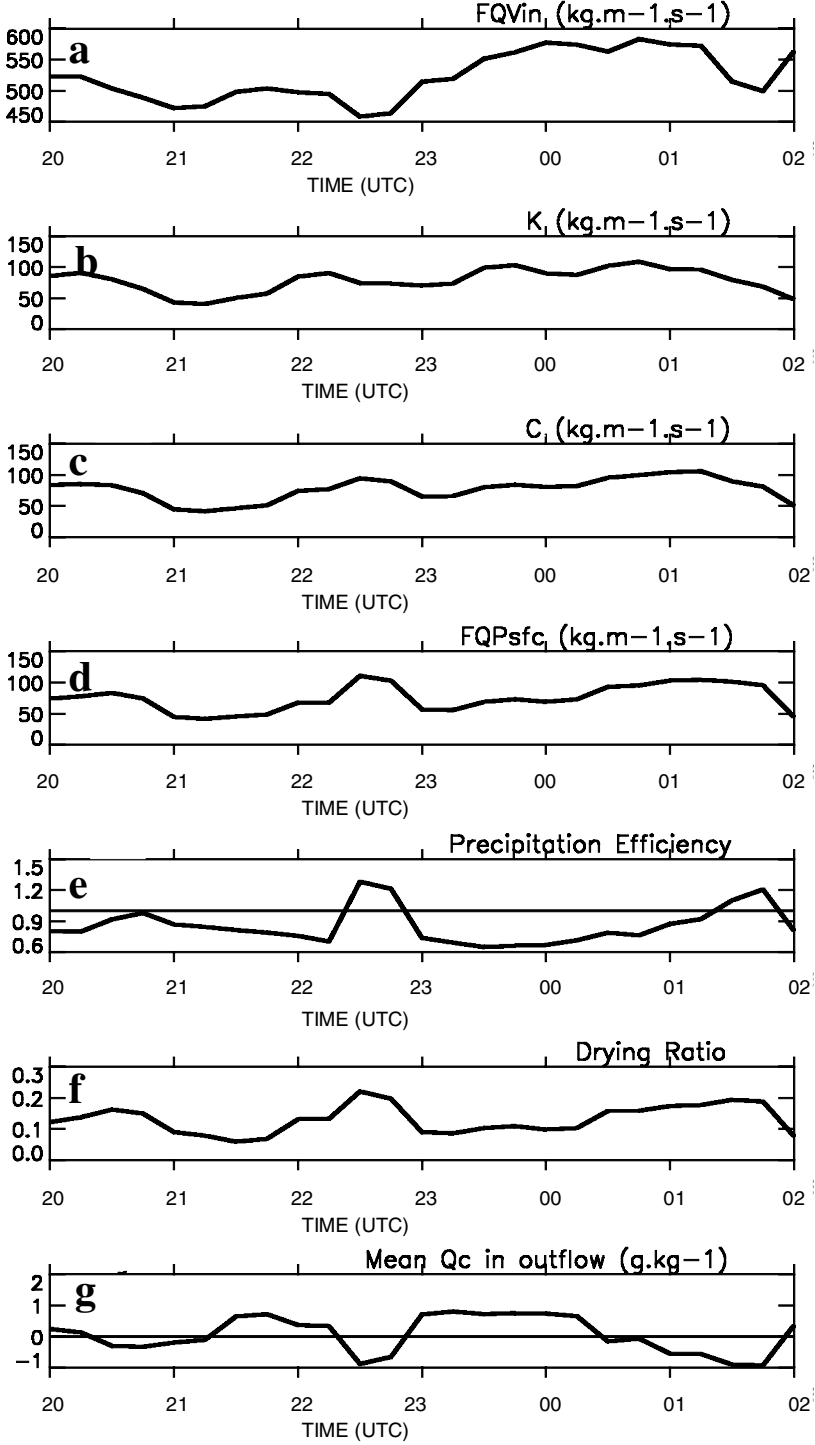


Figure 15. Evolution of the different elements of the two-dimensional water budget: (a) moisture inflow FQV_{in} , (b) condensation rate K , (c) conversion rate C , (d) surface precipitation rate FQP_{sfc} , (all in $\text{kg m}^{-1}\text{s}^{-1}$); (e) precipitation efficiency EFF , (f) drying ratio DR , (g) mean cloud-water content in outflow $\langle QC \rangle$ (g kg^{-1}).

The mean precipitation efficiency EFF (Fig. 15(e)) is defined here as:

$$EFF = FQP_{\text{sfc}} / (FQP_{\text{in}} + FQP_{\text{top}} + K).$$

It indicates the instantaneous ratio of condensed water plus inflowing precipitation that arrived at surface level (in fact, at the first level where reflectivity values were available, i.e. 100 to 400 m above surface level). The mean value for the period considered is 0.85 which is rather high but not surprising when considering that the moist environment inhibits strong evaporation, and that the relatively homogeneous horizontal wind allowed cloud water to grow smoothly into precipitation. Since the 0 °C isotherm was located near 3 km altitude (Fig. 4), collision-coalescence processes were probably efficient, though polarimetric S-Pol measurements revealed the presence of graupel aloft which indicates that riming of supercooled cloud droplets into graupel and melting into rain could also be important (Houze and Medina 2000; Yuter and Houze 2001, 2003). Values of EFF larger than 1 (from 2123 till 2154 and from 0124 till 0157 UTC) indicate that, for limited periods of time (generally when the surface precipitation rate was a maximum), more rain precipitated than cloud condensed. During these periods the cloud reservoir diminished.

The ‘drying ratio’, $DR = (FQP_{\text{sfc}} - FQP_{\text{in}} - FQP_{\text{top}}) / FQV_{\text{in}}$, indicates the proportion of water-vapour influx which transformed into precipitation. As seen in Fig. 15(f), the mean value was about 0.14, which is on the lower side of the estimates deduced by Smith *et al.* (2001) from numerical model analyses of IOP 2b within domains larger than the box shown in Fig. 11. Variations with time reveal that the drying ratio was mainly controlled by the surface precipitation rate with higher values ($DR \geq 0.18$) for intense precipitation ($FQP_{\text{sfc}} > 90 \text{ kg m}^{-1}\text{s}^{-1}$) and moderate moisture inflow ($450 < FQV_{\text{in}} < 520 \text{ kg m}^{-1}\text{s}^{-1}$), and smaller values ($DR \leq 0.10$) for weaker precipitation ($FQP_{\text{sfc}} < 50 \text{ kg m}^{-1}\text{s}^{-1}$) and slightly stronger moisture inflow ($470 < FQV_{\text{in}} < 560 \text{ kg m}^{-1}\text{s}^{-1}$).

Not all the terms on the left-hand sides of (4) and (5) can be calculated from the wind and reflectivity fields. Hence, we supposed that FQV_{in} can be estimated from the environmental humidity profile given by the radiosounding at Milano at 0000 UTC 20 September, and that FQC_{in} is equal to zero. These simple assumptions certainly led to underestimation of the water inflow (vapour FQV_{in} and cloud FQC_{in}) in the considered domain. As a matter of fact, the presence of precipitation in the outflow at $x = +27 \text{ km}$ (Fig. 13) indicates that air was probably saturated and contained some amount of non-precipitating cloud water or ice. It is possible to evaluate the consistency of (4) and (5) through the value of the mean cloud-water content in the outflow $\langle QC_{\text{out}} \rangle$ obtained as:

$$\langle QC_{\text{out}} \rangle = (FQV_{\text{in}} - C + E - FQS_{\text{out}}) / FM_{\text{out}} \quad (7)$$

with

$$FM_{\text{out}} = \int_{h_{2D}(x=27 \text{ km})}^{z_{\text{top}}(x=27 \text{ km})} \rho(z) u_{2D}(x = 27 \text{ km}, z) dz,$$

where FQS_{out} is the saturated moisture outflow (the saturated water-vapour content is deduced from the environmental values and retrieved pressure and temperature perturbations). It is not surprising to find strong decreases of $\langle QC_{\text{out}} \rangle$ during periods of more intense precipitation and high precipitation efficiency. However, the presence of unsaturated air in the outflow, i.e. negative values of $\langle QC_{\text{out}} \rangle$, might not be realistic as precipitation is observed there. This could be an artefact resulting from too dry an inflow FQV_{in} . Since C and E are fixed in (7), increasing FQV_{in} would lead to an identical increase of FQV_{out} . It seems, therefore, more realistic to suppose that an additional 1 to

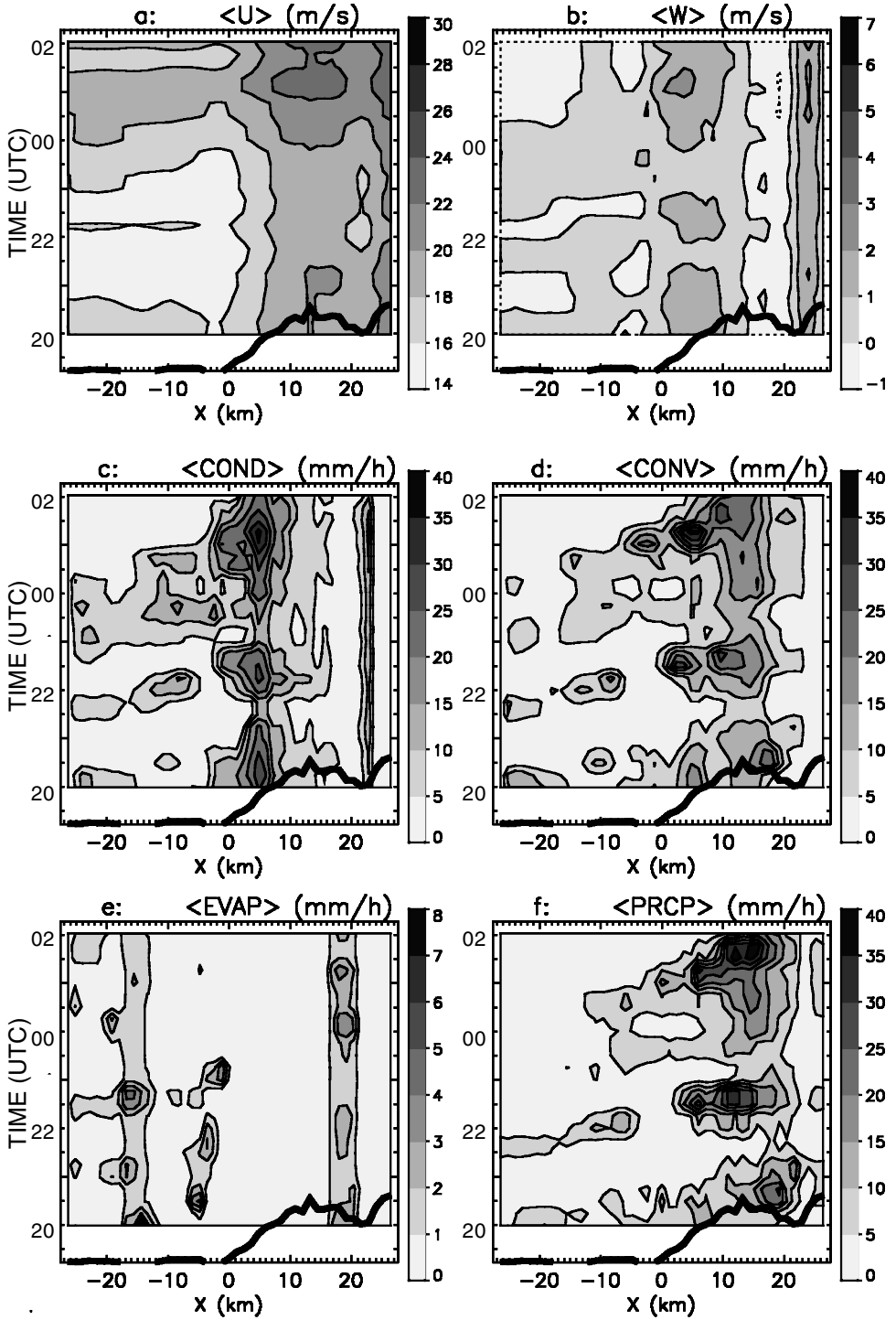


Figure 16. Time-distance distribution of: (a) density-weighted mean horizontal velocity (m s^{-1}), (b) density-weighted mean vertical velocity (m s^{-1}), (c) vertically integrated condensation rate (mm h^{-1}), (d) vertically integrated conversion rate (mm h^{-1}), (e) vertically integrated evaporation rate (mm h^{-1}), (f) surface precipitation rate (mm h^{-1}).

2 g kg⁻¹ of water vapour (up to the saturation value) or cloud water (above saturation) could be added to the inflow. This small modification would not change the results discussed above, except for the drying ratio which would be slightly smaller.

The relations between space and time distributions of horizontal and vertical wind, condensation, conversion and precipitation rates (expressed in mm h⁻¹) are shown in Fig. 16. Here, each quantity (except precipitation rate) represents a vertical integral between $h(x)$ and $z_{\text{top}}(x)$ and is displayed with respect to its location along x and its time of observation. Not surprisingly (e.g. Grossman and Durran 1984), the mean horizontal wind was stronger (18–20 m s⁻¹) over the mountains ($x > +5$ km) than over the plain where its velocity was 14–16 m s⁻¹ (Fig. 16(a)). Likewise, upward motions of 1–2 m s⁻¹ were found over the upward slope ($0 < x < +12$ km; Fig. 16(b)). Perturbations with respect to this mean structure show a relation between convergence induced by acceleration of the inflow at 2200 and 2300–0000 UTC, regions of weak ascending motions (0–1 m s⁻¹) over the plain and slightly stronger updraughts over the mountains. This is more easily seen on the plots of condensation (Fig. 16(c)), conversion (Fig. 16(d)) and precipitation (Fig. 16(f)) rates. Though relatively weak, the convergence-induced upward motions over the plain led to the formation of cloud water and ice, which was then transported horizontally and transformed into precipitation downstream. These rates increased from 5–15 mm h⁻¹ over the plain to 15–30 mm h⁻¹ over the mountain. Evaporation rates (Fig. 16(e)) were weaker (<5 mm h⁻¹) and were concentrated above the downward terrain slopes ($-18 < x < -14$ km, $-8 < x < -3$ km, $+16 < x < +21$ km). Weak condensation and precipitation rates were observed near the north-western limit of the domain ($x > +22$ km), due to the forced lifting of air that has already been substantially dried by previous ascent and condensation along the upwind slope. The propagation speed of the precipitating cells over the plain was 10 ± 4 m s⁻¹, and the distance between the maximum condensation rates (over the upwind slope) and precipitation rates (over the mountain top) was about 8 km, implying an advective time-scale of 10–20 minutes. As outlined by Smith *et al.* (2001), this is close to characteristic microphysical time-scale and probably explains the strong orographic impact on precipitation in this region.

5. CONCLUSIONS

Data collected during MAP IOP 2b by RONSARD, S-Pol and Monte-Lema ground-based Doppler radars near Lago Maggiore from 1900 UTC 19 September until 1100 UTC 20 September 1999 have been analysed using the RAMDAM procedure (Chong *et al.* 2000). This period was associated with one of the most intense rainfall events during the whole SOP and it showed characteristics that have frequently been observed during previous flooding situations in this region.

The synoptic conditions were marked by the passage of a north–south oriented frontal system over the Alps. Ahead of the cold front which was located approximately over central France at 0000 UTC 20 September, a strong south to south-easterly flow was blowing in the low levels over the Po Valley and the Lago Maggiore region, as is often observed for autumn precipitation events occurring in this area (Houze *et al.* 2001). Over the Po Valley and along the southern flank of the western Alps, there was a convergence between the easterly winds carrying warm and moist air from the Adriatic sea and the southerly flow with relatively drier air from the Mediterranean Sea. Such conditions were favourable for the development of precipitation.

The wind and precipitation fields derived from multi-Doppler analyses show that the strongest periods of precipitation observed during the considered period were

associated and collocated with intensifying low-level easterly wind components over the Po Valley and over the adjacent mountainous area. This can be explained by enhancement of convergence over the plain and more favourable orientation of the low-level flow with respect to the terrain slopes. Furthermore, convective cells over the Po Valley were advected toward the Alps where they induced more or less persistent rainfall over the mountains, while more variable precipitation occurred over the plain. This situation is different from that deduced by Rotunno and Ferretti (2001) for the PF of November 1994.

A relatively good agreement was observed between the reflectivity-derived and rain-gauge-observed precipitation rates. The analysis of the different terms of the water budget in a two-dimensional vertical cross-section extending from the plain to the mountains shows that the period of interest (from 2000 UTC 19 September to 0200 UTC 20 September) was characterized by varying moisture inflow, condensation, conversion and precipitation rates. Precipitation efficiency (the ratio between precipitation and condensation rates) was about 0.8 during periods of weak precipitation (mean value $< 4 \text{ mm h}^{-1}$), and 1.2 during stronger rainfall ($> 5.5 \text{ mm h}^{-1}$). Likewise, the drying ratio (the ratio between surface rainfall and moisture inflow) varied from < 0.10 during weak precipitation to > 0.14 during stronger precipitation. The space and time analysis of the condensation, conversion and precipitation rates reveals that condensation occurred preferentially over the upwind slope with, however, an important modulation by condensation over the plain; also precipitation was a maximum over the first mountain top as pointed out by Houze and Medina (2001) and Medina and Houze (2003), with an advective time-scale of 10–20 minutes which is close to the typical microphysical time-scale. Further comparisons with numerical modelling results (e.g. Asencio *et al.* 2003) will certainly help to better understand the influence of orography on intensity and distribution of rainfall.

ACKNOWLEDGEMENTS

We are indebted to the scientific and technical staffs who efficiently operated the RONSARD, S-Pol and Monte-Lema radars during the MAP SOP. This study was supported by grants from Programme ‘Atmosphère Océan à Moyenne Echelle’ from Institut National des Sciences de l’Univers et de l’Environnement. Esther Häller (ETH Zürich/MAP Data Center, Switzerland), Bob Rilling (NCAR/Atmospheric Technology Division, Boulder, Co., USA) and Georges Scialom (CETP, Vélizy, France) kindly provided the data from Monte-Lema, S-Pol and RONSARD radars, respectively. The comments made by two anonymous reviewers and the Editor helped to substantially improve the manuscript.

REFERENCES

- | | | |
|--|------|--|
| Asencio, N., Stein, J., Chong, M. and Gheuzi, F. | 2003 | Analysis and simulation of local and regional conditions for the rainfall over the Lago Maggiore Target Area during MAP IOP 2b. <i>Q. J. R. Meteorol. Soc.</i> , 129 , 565–586 |
| Austin, P. M. | 1987 | Relation between radar reflectivity and surface rainfall. <i>Mon. Weather Rev.</i> , 115 , 1053–1070 |
| Binder, P. and Schär, C. Eds. | 1996 | ‘MAP design proposal’. Available from MAP Programme Office, MeteoSwiss, CH-8044, Zürich, Switzerland, and URL: http://www.map.ethz.ch/proposal.htm |
| Bougeault, P., Binder, P., Buzzi, A., Dirks, R., Houze, R., Kuettner, J., Smith, R. B., Steinacker, R. and Volkert, H. | 2001 | The Map Special Observing Period. <i>Bull. Am. Meteorol. Soc.</i> , 82 , 433–462 |

- Buzzi, A. and Foschini, L. 2000 Mesoscale meteorological features associated with heavy precipitation in the southern Alpine region. *Meteorol. Atmos. Phys.*, **72**, 131–146
- Buzzi, A., Tartaglione, N. and Malguzzi, P. 1998 Numerical simulations of the 1994 Piedmont flood: Role of orography and moist processes. *Mon. Weather Rev.*, **126**, 2369–2383
- Chong, M., Georgis, J.-F., Bousquet, O., Brodzik, S. R., Burghart, C., Cosma, S., Germann, U., Gouget, V., Houze Jr, R. A., James, C. N., Prieur, S., Rotunno, R., Roux, F., Vivekanandan, J. and Zeng, Z. X. 2000 Real-time wind synthesis from Doppler radar observations during the Mesoscale Alpine Programme. *Bull. Am. Meteorol. Soc.*, **81**, 2953–2962
- Doswell, C. A. III, Brooks, H. E. and Maddox, R. A. 1996 Flash flood forecasting: An ingredients-based methodology. *Weather Forecasting*, **11**, 560–581
- Doswell, C. A. III, Ramis, C., Romero, R. and Alonso, S. 1998 A diagnostic study of three heavy precipitation episodes in the western Mediterranean region. *Weather Forecasting*, **13**, 102–124
- Ferretti, R., Low-Nam, S. and Rotunno, R. 2000 Numerical simulations of the Piedmont flood of 4–6 November 1994. *Tellus*, **52A**, 162–180
- Frei, C. and Schär, C. 1998 A precipitation climatology of the Alps from high-resolution rain-gauge observations. *Int. J. Climatol.*, **18**, 873–900
- Germann, U. and Joss, J. 2001 Variograms of radar reflectivity to describe spatial continuity of Alpine precipitation. *J. Appl. Meteorol.*, **40**, 1042–1059
- Grossman, R. L. and Durrán, D. R. 1984 Interaction of low-level flow with the western Ghat Mountains and offshore convection in the summer monsoon. *Mon. Weather Rev.*, **112**, 652–672
- Houze Jr, R. A. 1993 *Cloud dynamics*. Academic Press, San Diego, USA
- Houze Jr, R. A. and Medina, S. 2000 ‘Two cases of heavy rain on the Mediterranean side of the Alps in MAP’. Pp. 1–5 in Pre-prints of the ninth conference on mountain meteorology, Aspen, Co. American Meteorological Society, Boston, USA
- 2001 ‘Alpine precipitation mechanisms in MAP IOP 2b and 8’. Pp. 47–50 in MAP Newsletter No. 15. MeteoSwiss, CH-8044, Zürich, Switzerland. Also available at URL: <http://www.map.ethz.ch/NL15/houze.pdf>
- Houze Jr, R. A., James, C. N. and Medina, S. 2001 Radar observations of precipitation and airflow on the Mediterranean side of the Alps: Autumn 1998 and 1999. *Q. J. R. Meteorol. Soc.*, **127**, 2537–2558
- Lin, Y. L., Chiao, S., Wang, T. A., Kaplan, M. and Weglarz, R. 2001 Some common ingredients for heavy orographic rainfall. *Weather Forecasting*, **16**, 633–660
- Marshall, J. S. and Palmer, W. M. K. 1948 The distribution of raindrops with size. *J. Meteorol.*, **5**, 165–166
- Massacand, A. C., Wernli, H. and Davies, H. C. 1998 Heavy precipitation on the Alpine southside: An upper-level precursor. *Geophys. Res. Lett.*, **25**, 1435–1438
- Medina, S. and Houze Jr, R. A. 2003 Air motions and precipitation growth in Alpine storms. *Q. J. R. Meteorol. Soc.*, **129**, 345–371
- Rotunno, R. and Ferretti, R. 2001 Mechanisms of intense Alpine rainfall. *J. Atmos. Sci.*, **58**, 1732–1749
- Roux, F., Marécal, V. and Hauser, D. 1993 The 12/13 January 1987 narrow cold-frontal rainband observed during MFDP/FRONTS 87. Part I: Kinematics and thermodynamics. *J. Atmos. Sci.*, **50**, 951–974
- Sekhon, R. S. and Srivastava, R. C. 1970 Snow size spectra and radar reflectivity. *J. Atmos. Sci.*, **27**, 299–307
- 1971 Doppler radar observations of drop-size distribution in a thunderstorm. *J. Atmos. Sci.*, **28**, 983–994
- Smith, R. B. 1979 The influence of mountains on the atmosphere. *Adv. Geophys.*, **21**, 87–230
- 1989 Hydrostatic airflow over mountains. *Adv. Geophys.*, **31**, 1–41
- Smith, R. B., Jiang, Q., Fearon, M., Doyle, J. D. and Benoit, R. 2001 ‘Orographic precipitation and air mass drying over the Alps: Preliminary results from MAP IOP 2b’. Pp. 65–68 in MAP Newsletter No. 15, MeteoSwiss, CH-8044, Zürich, Switzerland (Also available at URL: http://www.map.ethz.ch/NL15/smith_oron_oral.pdf)

